Kinematic Observations of Misocyclones along Boundaries during IHOP

JAMES N. MARQUIS AND YVETTE P. RICHARDSON

Department of Meteorology, The Pennsylvania State University, University Park, Pennsylvania

JOSHUA M. WURMAN

Center for Severe Weather Research, Boulder, Colorado

(Manuscript received 21 March 2006, in final form 4 August 2006)

ABSTRACT

During the International H_2O Project, mobile radars collected high-resolution data of several 0.5–2-km-wide vertically oriented vortices (or misocyclones) along at least five mesoscale airmass boundaries. This study analyzes the properties of the misocyclones in three of these datasets—3, 10, and 19 June 2002—to verify findings from finescale numerical models and other past observations of misocyclones and to further the understanding of the role that they play in the initiation of deep moist convection and nonsupercell tornadoes. Misocyclones inflect or disjoint the swath of low-level convergence along each boundary to varying degrees depending on the size of their circulations. When several relatively large misocyclones are next to each other, the shape of low-level convergence along each boundary is arranged into a staircase pattern. Mergers of misocyclones are an important process in the evolution of the vorticity field, as a population of small vortices consolidates into a smaller number of larger ones. Additionally, merging misocyclones may affect the mixing of thermodynamic fields in their vicinity when the merger axis is perpendicular to the boundary. Misocyclones interact with linear and cellular structures in the planetary boundary layers (PBLs) of the air masses adjacent to each boundary. Cyclonic low-level vertical vorticity generated by both types of structures makes contact with each boundary and sometimes is incorporated into preexisting misocyclones. Intersections of either type of PBL structure with the boundary result in strengthened pockets of low-level convergence and, typically, strengthened misocyclones.

1. Introduction

As more high-resolution observations of storm environments become available, the roles that small-scale planetary boundary layer (PBL) phenomena play in the initiation of deep moist convection and subsequent severe weather can be elucidated. One such phenomenon is a misocyclone, defined in this study as a vertical vorticity maximum, with a diameter between 40 m and 4 km (Fujita 1981) that is found along a mesoscale airmass boundary (hereafter referred to as a boundary). Past studies have examined misocyclones along the leading edge of thunderstorm outflows (e.g., Fujita 1981; Mueller and Carbone 1987; Lee and Wilhelmson 1997a, hereafter LW97a; Kessinger et al. 1988; Roberts and Wilson 1995; Weckwerth and Wakimoto 1992; Friedrich et al. 2005), cold fronts (e.g., Wilson 1986; Carbone 1982), sea-breeze boundaries (e.g., Atkins et al. 1995; Kingsmill 1995), and other mesoscale convergence lines (e.g., Wilson 1986; Crook et al. 1991; Wilson et al. 1992, hereafter W92).

Misocyclones are thought to influence the initiation of deep moist convection [hereafter convection initiation (CI)]. For example, Lee et al. (2000) show that the presence of misocyclones along a simulated thunderstorm gust front produces moist convective updrafts that are deeper and more intense than those for an analogous gust front without misocyclones. They also show that misocyclones can locally enhance convergence and moisture fields along the gust front, helping to create isolated updrafts that can overcome the negative buoyancy associated with a capping inversion. In an observational study by W92, a series of convective clouds initiates with a very similar spacing to that of a population of misocyclones observed along the Denver convergence zone. However, while many studies show

Corresponding author address: James N. Marquis, 503 Walker Building, University Park, PA 16802.
E-mail: jmarquis@met.psu.edu

DOI: 10.1175/MWR3367.1

that areas along a boundary near misocyclones are preferred regions for CI (e.g., Weckwerth and Wakimoto 1992; Arnott et al. 2006, hereafter A06; Richardson et al. 2003; Murphey et al. 2006; Lee et al. 2000; W92), some (e.g., Kingsmill 1995; Friedrich et al. 2005) show evidence that they are not. Therefore, even with the previously studied collection of several CI datasets containing misocyclones, there is still some uncertainty as to whether they typically influence convective development.

Past studies also have shown that misocyclones can play an important role in the formation of certain nonsupercell tornadoes (NSTs; Wakimoto and Wilson 1989). These NSTs form when the rotation from a misocyclone is advected upward toward cloud base and is stretched into tornadic intensity by a nonrotating convective updraft (e.g., Carbone 1982, 1983; Forbes and Wakimoto 1983; Wilson 1986; Brady and Szoke 1989; Roberts and Wilson 1995).

The International H_2O Project (IHOP; Weckwerth et al. 2004), a field research campaign to study the mesoscale environments during CI (among other objectives), was conducted in the spring of 2002 on the U.S. plains. Data of uniquely high temporal and spatial resolution collected by mobile radars employed in IHOP allow us to observe, in great detail, seldom documented phenomena such as misocyclone mergers and the interactions between misocyclones and other organized motions in the planetary boundary layer (evident as linear or cellular features in radar reflectivity). Each IHOP mobile radar deployment typically lasted for several hours, allowing us to track the motion and behavior of individual misocyclones. This is valuable because few studies have documented the evolution of entire misocyclone populations, something that is shown in Lee and Wilhelmson (1997b, hereafter LW97b) to be of critical importance to NST formation (an example of which occurs on one of the IHOP days analyzed herein). Additionally, only a few studies (e.g., Friedrich et al. 2005; LW97a; Lee and Wilhelmson 2000) compare the behavior of misocyclones originating in several different environments, which is an important task because it highlights those environments most conducive to strong vortices.

The goal of this study is to provide unique observations regarding the kinematics and evolution of both individual and entire populations of misocyclones, with the hope that this knowledge will aid in our understanding of the role misocyclones play in CI and NSTs. We utilize radar-derived wind fields to address the following:

1) the kinematic structure of the IHOP misocyclones and their near environments,
2) the mergers of misocyclones and the evolution of entire misocyclone populations,
3) the observed interactions between the IHOP misocyclones and both linear and cellular structures in the PBL, and
4) a brief comparison of the horizontal shear and convergence along the three IHOP boundaries that produce misocyclones of different average intensities.

These observations are presented in section 3. Section 2 outlines the processing and objective analysis of the radar data. A summary is presented in section 4. An appendix is included to describe some of the methods by which objective 4 is accomplished.

2. Method

Dual- and multi-Doppler radar data collected by two Doppler on Wheels radars (DOWs; Wurman et al. 1997), the X-band polarimetric radar (XPOL; Wurman 2001), and the Shared Mobile Atmospheric Research and Teaching (SMART) radar (Biggerstaff and Guynes 2000; Biggerstaff et al. 2005) during IHOP on 3, 10, and 19 June 2002 are used in this study. Different deployment configurations of these radars were used on each day to achieve multi-Doppler wind synthesis in an area surrounding the boundaries. Radar sweep elevation angles ranged from 0.5° to 14.5°; low-level elevation increments were 0.5° and increased to 1.0° above 3.0° so that the greatest vertical detail was realized at the lowest levels. Great care was taken to ensure simultaneous data collection at a given elevation by all radars, with GPS timing used to synchronize volume start times every 3 min. While not all radar volumes were perfectly synchronized in this manner, the antenna scanning rate and elevation lists used by the DOWs and XPOL were such that a data volume was completed in 90 s, yielding a maximum 45-s time offset between scans from different radars at a particular elevation. Radar baselines were between 12 and 24 km, depending on the available road network and the spatial scale of the desired observation domain. For further details of the radar deployments on 3, 10, and 19 June, the reader is referred to Stonitsch and Markowski (2007, hereafter SM07), A06, and Richardson et al. (2003), respectively.

Raw radar data were edited in the following ways.

1) The sweeps were rotated to an earth-relative reference frame using a solar alignment technique discussed in Arnott et al. (2003). When no solar alignment scan was available, data were rotated by aligning ground clutter in the lowest elevation scans with a database of the local road and tower networks.
2) Data gates with a normalized coherent power value

TABLE 1. Summary of objective analysis parameters used for all three datasets. Here Δ is the Cartesian grid spacing, κ is the Barnes smoothing parameter, and R_c is the cutoff radius; $\lambda_{0.25}$, $\lambda_{0.5}$, and $\lambda_{0.75}$ are the wavelengths (km) corresponding to a 25%, 50%, and 75% theoretical response, respectively, of the Barnes filter used on each day; and $\overline{u}_{\text{ref}}$ and $\overline{v}_{\text{ref}}$ are the east–west and north–south components, respectively, of the height- and daily averaged reference velocity vector.

Day	Δ (km)	κ (km^2)	R_c (km)	$\lambda_{0.25}$ (km)	$\lambda_{0.5}$ (km)	$\lambda_{0.75}$ (km)	$\overline{u}_{\text{ref}}$ (m s^{-1})	$\overline{v}_{\text{ref}}$ (m s^{-1})
3 Jun	0.125	0.250	0.650	1.3	1.9	2.9	5.0	2.0
10 Jun	0.100	0.263	0.889	1.4	1.9	3.0	2.6	5.0
19 Jun	0.150	0.320	0.750	1.5	2.1	3.3	4.0	6.9

less than 0.15–0.25 (different for each radar) were excluded from analysis.

3) Ground clutter contamination was removed using constraints on radar reflectivity and/or near-zero radial velocity.
4) Aliased velocities were unfolded.

Following Matejka (2002), a horizontal reference frame velocity vector $\mathbf{V}_{\text{ref}}$ was calculated to remove artificial tilting with height of observed features due to their motion between consecutive radar sweeps. Here $\mathbf{V}_{\text{ref}}$ was calculated at 20–45-min intervals on each day and at three evenly spaced heights with vertical interpolation in between (a height- and time-averaged value of the horizontal components of $\mathbf{V}_{\text{ref}}$ for each day is provided in Table 1). The height-dependent $\mathbf{V}_{\text{ref}}$ was used to adjust the horizontal position of each datum to its most likely location at a central time for each radar volume.

Edited radar volumes with the correct reference frames were objectively analyzed using an isotropic Barnes weighting function (Barnes 1964) with a smoothing parameter $\kappa = (1.33\delta)^2$ (Pauley and Wu 1990), where the observed data spacing $\delta = \theta R$ [θ is the beamwidth of the radar and R is the distance between a radar and the farthest edge of the desired analysis domain (Trapp and Doswell 2000)]. The beamwidths of the radars are 0.93° for the DOWs and XPOL and 1.5° for the SMART radar. The largest δ of all radars participating in one deployment was used to calculate κ for all radars in that deployment. A cutoff radius, $R_c \approx 3\delta$, similar to recommendations by Pauley and Wu (1990), was employed to decrease computational time during the objective analysis while still achieving approximately the theoretical response function. The data point spacing (Δ) of the Cartesian grid on which the radar data were objectively analyzed was chosen to be between $\delta/3$ and $\delta/2$ (Koch et al. 1983). The vertical depth of the Cartesian grid was typically near 1.5 km, due to poor radar data returns in the mid- to upper planetary boundary layer. Table 1 lists the objective analysis parameters used for the three datasets.

The 3D wind field was synthesized from the objectively analyzed data by an upward integration of the anelastic mass continuity equation. An iterative technique was used to adjust the u, v, and w fields until the change in the density-weighted w between iterations was less than 0.01 kg m^{-2} s^{-1}. A dual-Doppler solution was not calculated for a beam crossing angle of less than 30° or greater than 150°. When possible, a scheme for obtaining overdetermined dual-Doppler winds (Kessinger et al. 1987) was used. Because of the geometry of the radar deployments, dual-Doppler radar data sometimes were not available below z = 200–300 m AGL in the areas of interest, making the application of mass continuity to retrieve vertical velocity troublesome. Therefore, we often used low-level horizontal convergence ($-\nabla \cdot \mathbf{V}_h$) at z = 300 m AGL as the proxy for vertical velocity (e.g., low-level convergence equals upward motion). However, it is possible that the relationship between convergence and w is different than expected if the unobserved convergence/divergence near the surface is especially strong and opposite that observed at our lowest level. However, modeling studies provide no evidence that this is the case in the phenomena being studied here, except perhaps in misocyclones showing divergence at 300 m, which LW97a showed may often be accompanied by a thin layer of significant convergence near the surface. Outside of these particular phenomena, we expect the vertical velocity field of the lower boundary layer to be qualitatively similar to the convergence field at 300 m. The precise magnitude of w is sensitive to the height at which the lower boundary condition is applied (e.g., w differences of 1–2 m s^{-1} are found at 500 m AGL when $w = 0$ is asserted at $z = 0$, which requires downward extrapolation of radial velocities, versus z = 250 m). When a calculation of w was required (e.g., for trajectory analysis), $w = 0$ was asserted at the ground and downward extrapolation of kinematic data was performed. The horizontal displacement following trajectories of interest in this study shows very little sensitivity to these assumptions.

IHOP case descriptions

A brief discussion of the mesoscale settings of 3, 10, and 19 June as they pertain to the radar deployments

and the misocyclone analysis is provided here. The reader is again directed to SM07, A06, Richardson et al. (2003), and Murphey et al. (2006) for more detailed synoptic and mesoscale discussions pertaining to convection initiation on these days.

On 3 June, DOW 2, DOW 3, XPOL, and the SMART radar observed an ENE–WSW-oriented cold front in the eastern Oklahoma panhandle. The radar data used in this study are from 1615 to 1815 UTC (all times hereafter are rounded to the nearest minute unless otherwise mentioned). Several relatively weak misocyclones and misocyclone mergers are observed on this day.

On 10 June, DOW 2, DOW 3, XPOL, and the SMART radar observed a NE–SW-oriented quasi-stationary front near Ness City, Kansas. The data used in this study are from 1930 to 2120 UTC. Several misocyclones of moderate intensity along with misocyclone mergers are observed on this day.

On 19 June, DOW 2, DOW 3, and XPOL observed a NNE–SSW-oriented dryline near Colby, Kansas. Mobile radar data are available from 1920 to 2345 UTC, during which extensive misocyclone activity is observed, including several strong misocyclones and many striking mergers. An NST ($\zeta \approx 10^{-1}$ s^{-1}) that was presumably spawned by the interaction of a moist convective cell with a misocyclone was observed by DOW3 near 0000 UTC.

3. Results

We first examine a typical IHOP misocyclone (Fig. 1). Most misocyclones from the three IHOP datasets exhibit similar structure. A maximum in vertical vorticity is collocated with a radar reflectivity maximum.[1] The boundary near the misocyclone, indicated by a linear swath in reflectivity, is kinked or inflected by the circulation of air around the center of rotation. The contours of vertical vorticity in the misocyclone exhibit a quasi-circular shape, except during interactions with neighboring misocyclones when they often deform into ellipses. The vertical vorticity field decreases with height (Fig. 1b) and sometimes extends beyond the highest altitude well observed by the radars (roughly half of the depth of the mixed planetary boundary layer on each day). The horizontal convergence field, while generally positive along the boundary, is often minimized within the core of rotation. This is likely due to

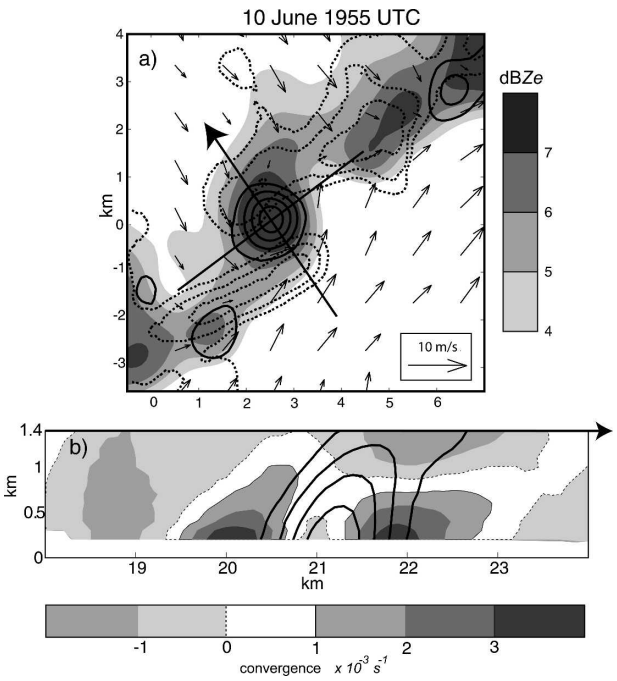

FIG. 1. Kinematic structure of a misocyclone at 1955 UTC 10 Jun. Vertical vorticity is shown in solid black contours. The outermost contour is 4×10^{-3} s^{-1}, incremented by 3×10^{-3} s^{-1}. (a) A horizontal plane view at 300 m AGL with contours of convergence (dashed), misocyclone-relative horizontal winds (vectors), and radar reflectivity from DOW 2 (shaded). The outermost contour of convergence is 1.2×10^{-3} s^{-1}, incremented by 1×10^{-3} s^{-1}. Boldface lines are provided to illustrate the misocyclone-relative quadrants discussed in the text. (b) The convergence field (shaded) in the vertical cross section through the across-front boldface line in (a), oriented in the direction of the arrow head. The white area below approximately 250 m is missing data.

a downward-oriented perturbation pressure gradient force associated with a negative vertical gradient of the magnitude of vertical vorticity (e.g., Klemp and Rotunno 1983). This feature has been shown in many atmospheric vortices, including misocyclones (e.g., Markowski and Hannon 2006, hereafter MH06; LW97a; Murphey et al. 2006). The common occurrence of low-level divergence in the center of misocyclones often yields negative or near-zero values of relative helicity there (consistent with MH06), suggesting that the turbulent dilution of vertical momentum is not inhibited within them (contrary to the hypothesis of Pietrycha and Rasmussen 2004).

At 2154 UTC 19 June, DOW 3 collected very high resolution (13- and 32-m radial and azimuthal spacing, respectively) single-Doppler data of a misocyclone at approximately a 2-km range. The 0.5° elevation radar sweep is shown in Fig. 2. Contrary to the structure observed at greater range, radar reflectivity is minimized in the core of rotation, possibly similar to the echo-free

[1] Clear-air reflectivity in all three cases is assumed to be power reflected from lofted particulate scatterers and insects that approximately follow the surrounding airflow.

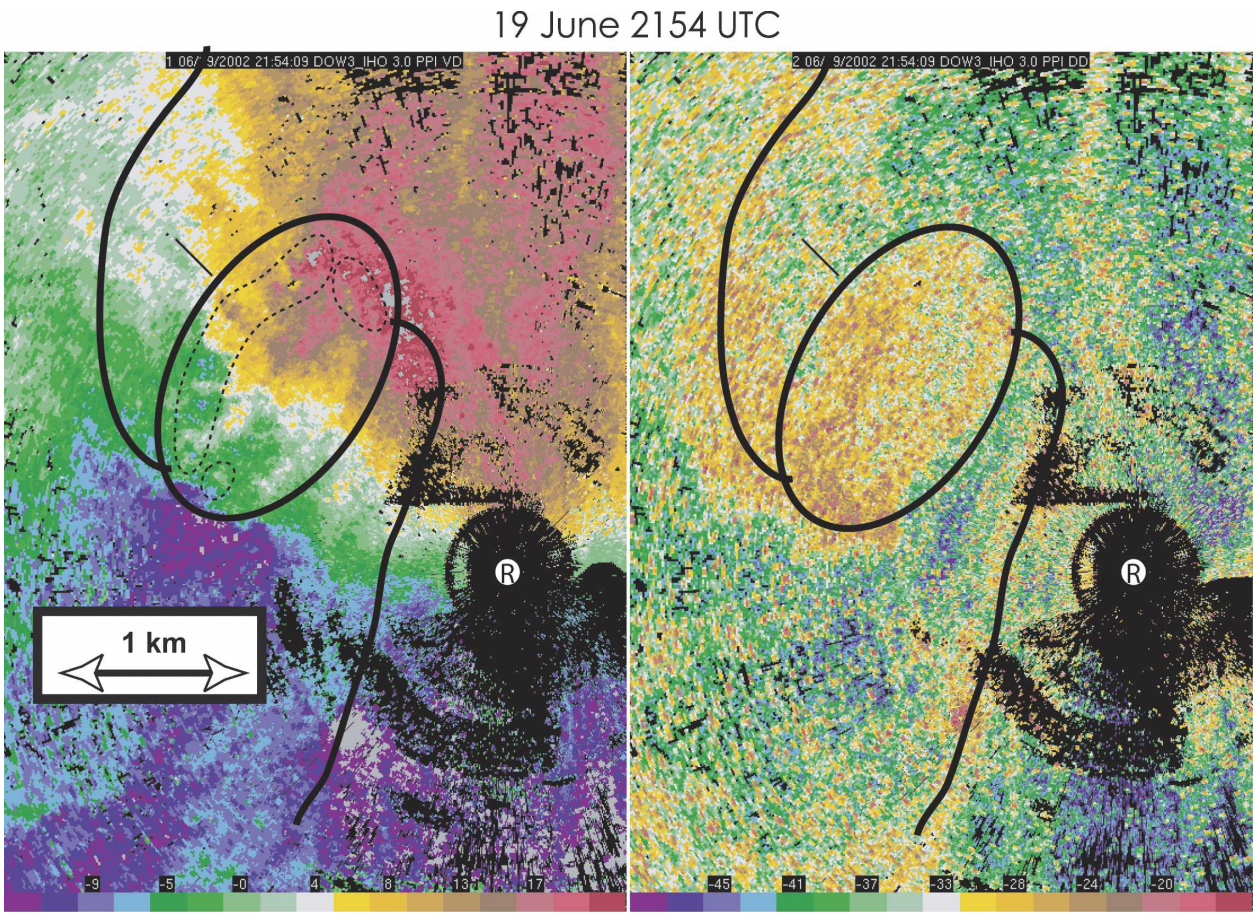

FIG. 2. (left) Radial wind and (right) radar reflectivity at the 0.5° elevation angle sweep from DOW 3 at 2154 UTC 19 Jun in a misocyclone that is at approximately the 2-km range. The dashed contours on the left indicate regions in which locally strong areas of azimuthal shear of the radial wind are located. The solid black contours outline the radar reflectivity field along the dryline and in the misocyclone. An "R" marks the location of DOW 3 in each image.

eye seen in high-resolution radar observations of tornadoes (e.g., Wurman et al. 1996; Bluestein and Pazmany 2000; Dowell et al. 2005). The overall shape of the misocyclone at this time is elliptical, consistent with a vortex that has recently merged with a nearby neighbor. Small-scale (~100 m) velocity structures present within the reflectivity annulus resemble small, weak, dust devil–like vortices.

a. Misocyclones and low-level mesoscale convergence

The IHOP misocyclones distort the shape of the low-level convergence field near their locations along each boundary, likely due to the advection of environmental momentum around the center of rotation. In Fig. 1a, mesoscale convergence near the misocyclone is present in roughly two quadrants relative to the maximum in vertical vorticity. The overall pattern of low-level convergence at a boundary often resembles a "staircase" shape when neighboring misocyclones are each similarly manipulating the nearby mesoscale convergence into two quadrants; each two-quadrant shape resembles an individual "step" in the staircase. An example of this staircase pattern is shown in Fig. 3a, along with an example shown by LW97b (Fig. 3b) that it closely resembles.

Mesoscale convergence is present with varying degrees of distortion near all of the IHOP misocyclones. Some misocyclones highly distort the boundary (e.g., the two-quadrant step described above), while some do not appear to distort it significantly. Figure 4 schematically illustrates this continuum of amplitudes of distortion observed near misocyclones. The highest-amplitude distortions of the convergence and reflectivity bands near individual misocyclones are seen in the first half of the 10 June data. The highest-amplitude distortions overall occur throughout all three datasets when misocyclones are merging with an orientation

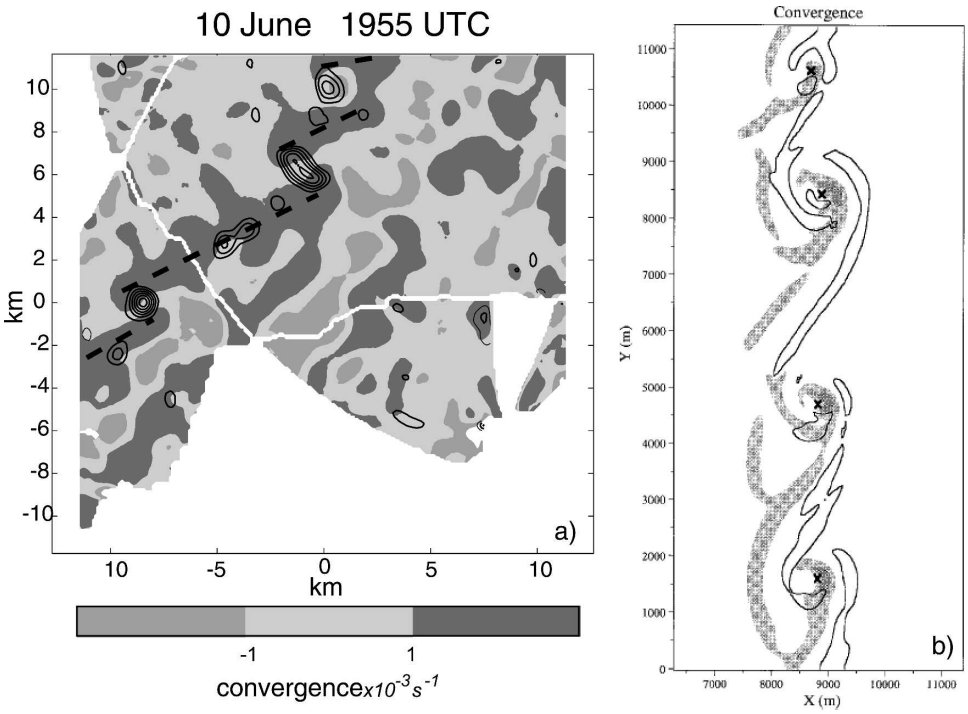

FIG. 3. (a) A staircase pattern of convergence (shaded) and vertical vorticity (contours) at 300 m AGL along the front at 1955 UTC 10 Jun. The outermost contour of vertical vorticity on the left is 4×10^{-3} s^{-1}, incremented by 2×10^{-3} s^{-1}. Missing data are white. (b) The convergence near four misocyclones (NSTs) indicated by Xs along a gust front from LW97b. Surface convergence greater than 0.01 s^{-1} is shaded and 500-m-AGL convergence of 0.01 s^{-1} is contoured.

that is perpendicular to the average orientation of the mesoscale boundary. While it is difficult to calculate the width of mesoscale convergence across each boundary near a misocyclone because of its deformed shape, the average width of the boundary far from the influence of any misocyclones is narrowest (approximately 1–1.5 km) in the first half of 10 June. Throughout most of that day, misocyclone diameters are generally greater than 1.2 km. Misocyclone diameter is defined as the distance between positive and negative extrema in unsmoothed radial velocity data collected by the closest radar (to minimize artificial widening due to beam spreading). There are many times in all three datasets when low-amplitude convergence distortions are found next to higher-amplitude distortions. The low-amplitude distortions are associated with individual misocyclones, whereas those of higher amplitude are seen near merging misocyclones that are increasing the circulation length scale in the across-boundary direction (discussed in greater detail later). Therefore, it appears that the size of the misocyclonic circulation relative to the width of mesoscale convergence controls the amplitude of distortion of the boundary. The vertical motion field along a boundary is often fractured when a misocyclone highly distorts the mesoscale convergence field and breaks its continuity with divergence in the core of rotation [as in A06; MH06; SM07; LW97a; and mesovortices embedded in squall lines simulated by Trapp and Weisman (2003)].

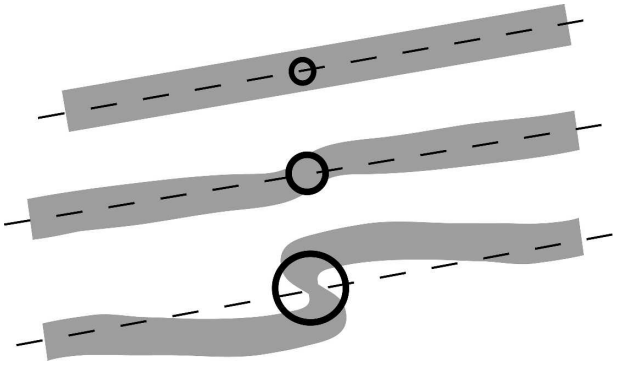

FIG. 4. A schematic representation of the continuum of distortion amplitude along a boundary near a misocyclone. Negligible distortion is at the top and high-amplitude distortion is at the bottom. Positive mesoscale convergence along the boundary is shaded. The dark black rings denote the radius of peak tangential winds of a misocyclone. Dashed lines represent the overall orientation of the boundary (a line tracing the center of the convergence swath along the boundary far from misocyclone influence). For simplicity, areas of misocyclone-enhanced convergence are not shown.

In Fig. 1a, the strength of convergence along the front in each of the two quadrants relative to the misocyclone is approximately equal. However, this is not always observed. Near many misocyclones, convergence is enhanced on only one side, while near others, neither side is enhanced significantly above the average value along the boundary. An example from 3 June is shown in Fig. 5 in which the magnitude of the convergence field near three misocyclones is enhanced downstream (relative to the flow in the frontal zone) of each misocyclone. In this example, the enhanced convergence field appears to be roughly one-quarter wavelength out of phase with the vertical vorticity field, consistent with Kingsmill (1995) and airborne radar observations of the dryline on 19 June 2002 (Murphey et al. 2006). Misocyclones surrounded by convergence on all sides (i.e., misocyclones that negligibly distort the boundary) often do not enhance the nearby mesoscale convergence field.

It is unclear why pockets of enhanced convergence are found upstream, downstream, upstream and downstream, or not at all along boundaries near misocyclones. It is possible that localized frontogenesis caused by a misocyclone (Doswell 1984; Davies-Jones 1985; Pietrycha and Rasmussen 2004) enhances vertical motion by increasing the horizontal buoyancy gradient. This hypothesis will be tested more extensively in a future study using mobile mesonet and rawinsonde observations collected during IHOP. The reader may question which came first: the convergence or the misocyclone? Pockets of enhanced convergence and upward motion are found near the misocyclones of horizontal shearing instability origin in LW97a, whereas convergence along the gust front is approximately uniform prior to their formation. Therefore, misocyclones themselves may enhance pockets of convergence along many otherwise uniform boundaries. Intersections of linear PBL structures (e.g., horizontal convective rolls) with the boundary, which may enhance convergence near misocyclones (W92), are addressed in more detail later.

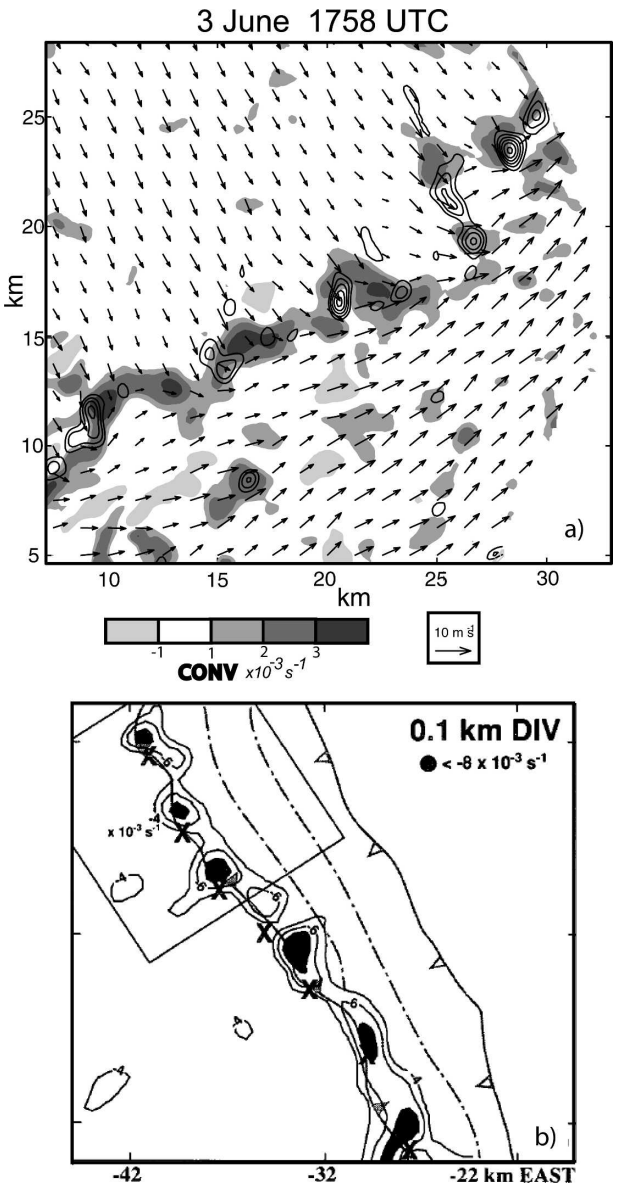

FIG. 5. (a) The convergence (shaded), vertical vorticity (contours), and ground relative wind (vectors) at 300 m AGL in the vicinity of the front at 1758 UTC 3 Jun. The outermost contour of vertical vorticity is 4×10^{-3} s^{-1}, incremented by 2×10^{-3} s^{-1}. (b) The divergence (contours and shaded) and vertical vorticity maxima (indicated by Xs) along a sea-breeze boundary from Kingsmill (1995).

b. Mergers of misocyclones

One of the most intriguing observations from the three IHOP datasets involves the consolidation of neighboring misocyclones. Figure 6 documents a chain of several merging misocyclones during a 1-h span along the dryline of 19 June. At the beginning of this sequence (Fig. 6a), several misocyclones with an average diameter of 0.7 km are paired along the dryline (e.g., misocyclone C is in close proximity to D, E to F, and G to H). By 2131 UTC (Fig. 6b), these paired misocyclones have merged, resulting in vortices with an average diameter of approximately 1.0 km. The resultant misocyclones (CD, EF, and GH) are evenly spaced along the boundary with an average separation of approximately 4.0 km. Additionally, I and J have entered the analysis domain from the south and will soon pair and merge. At 2146 UTC (Fig. 6c), this merger is complete and the resultant vortex, IJ, will soon merge with K at 2204 UTC (Fig. 6d). Once GH and IJK have merged, four misocyclones that are spaced 10–15 km

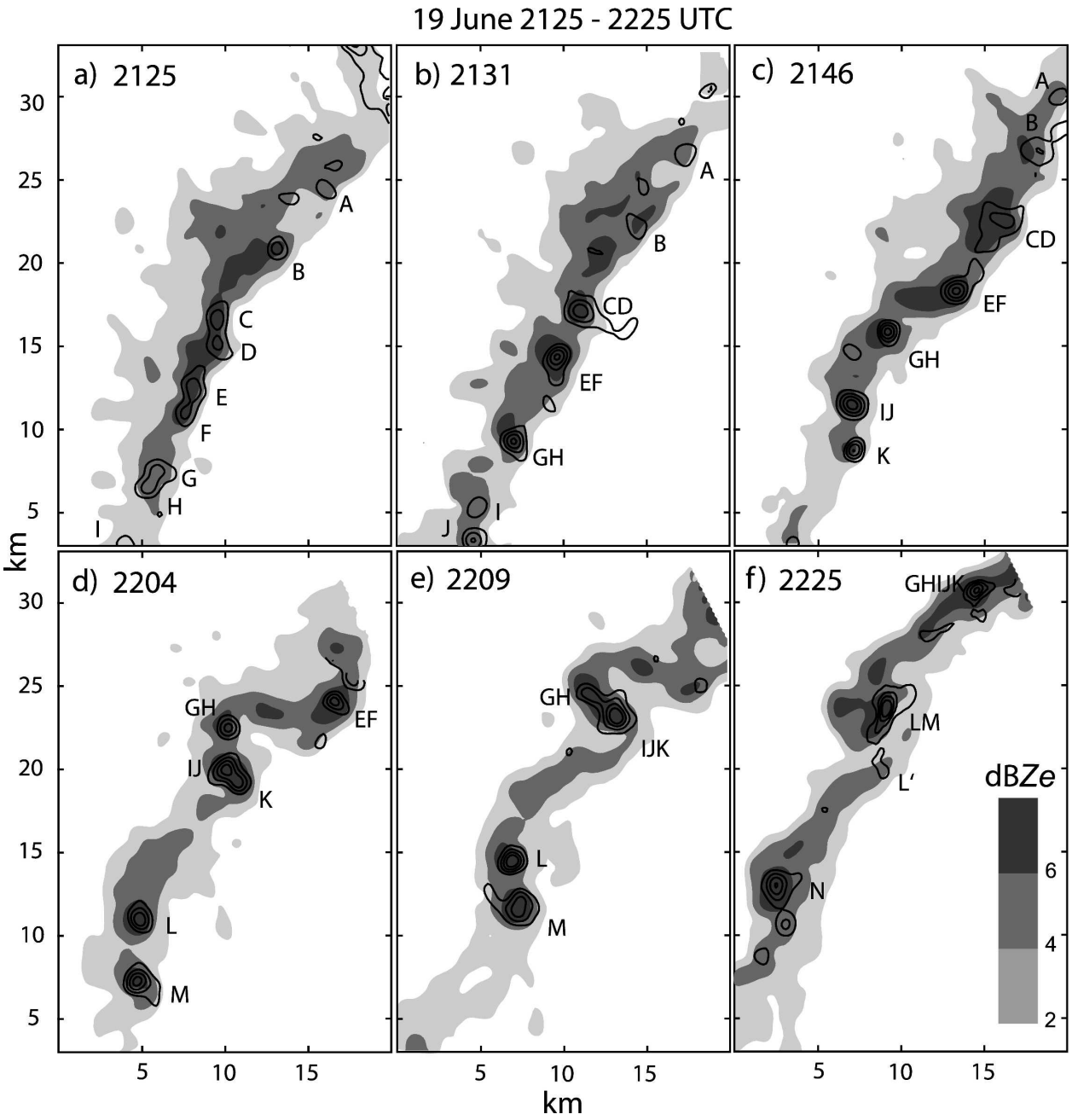

FIG. 6. Radar reflectivity (shaded) and vertical vorticity (contours) along the dryline at (a) 2125, (b) 2131, (c) 2146, (d) 2204, (e) 2209, and (f) 2225 UTC 19 Jun. Individual misocyclones are labeled by letter, and misocyclones resulting from mergers are labeled with the letters of all misocyclones participating in the merger. The L′ in (f) indicates vorticity from L that has not yet fully consolidated into LM. The outermost contours of vertical vorticity are 5×10^{-3} s^{-1}, incremented by 5×10^{-3} s^{-1}. Vorticity and reflectivity away from the dryline are excluded for simplicity. The subdomain shown is fixed in space; thus, individual misocyclone motions are toward the NNE.

apart are present in the analysis domain at 2225 UTC (Fig. 6f; misocyclone O not shown). At this time, the equivalent circular diameter of GHIJK is 1.2 km, indicating a 70% increase in diameter (again, measured using unsmoothed single-Doppler velocities) from misocyclones G, H, and I at 2125 UTC.

While many of the vortices observed at the dryline at 2225 UTC are not observed by the radars at 2125 UTC, it is clear that many vortices passing through the radar domain pair with their neighbors and merge, causing a decrease in the misocyclone population density and an increase in vortex diameter. The observation of merg-

ing misocyclones is consistent with the simulations of LW97a and with the merger of mesoscale vortices embedded in squall lines simulated by Weisman and Trapp (2003). Prior to 2125 UTC, several misocyclones with differing amplitudes of peak vertical vorticity and irregular spacing are present along the dryline; therefore, it may be coincidence that misocyclones C, D, E, F, G, and H have similar size, similar intensity, and regular spacing between pairs at 2125 UTC. Similar arguments can also be made for new misocyclones entering the domain throughout Fig. 6.

Misocyclones are present along each boundary at the beginning of radar observations on all 3 days; therefore, there is no observation of their production by means of a vortex sheet roll up as observed in LW97a and others (e.g., Miles and Howard 1964; Christiansen and Zabusky 1973; Manin 1992). The evolution of the vorticity field by way of vortex merger precludes relating misocyclone spacing along each boundary to the width of a presumed original shear zone as presented by Miles and Howard (1964). Therefore, it may not be possible to determine if horizontal shearing instability is the likely formation mechanism of the IHOP misocyclones.

Vertical vorticity contours during the merger of misocyclones L and M from Fig. 6 are shown with higher temporal resolution in Fig. 7. As L and M draw close between 2210:48 and 2218:45 UTC, their interacting circulations cause them to rotate about the center point of the merger axis (consistent with Fujiwhara 1931), a line segment connecting the centers of each misocyclone. This interaction continues throughout the rest of the merger. At 2221:47 UTC, the vorticity maxima of L and M are about one to two misocyclone diameters apart and their quasi-circular vorticity contours are deformed into elliptical shapes. A single misocyclone (LM) emerges a few minutes later, with its vorticity contours maintaining an elliptical shape. This particular misocyclone travels out of the observed domain without its vorticity contours returning to a quasi-circular shape. However, the shapes of other misocyclones resulting from mergers are observed to be quasi-circular several minutes after coalescence (e.g., CD, EF, and GH in Fig. 6b).

Mergers among the IHOP misocyclones are similar to the general descriptions of vortex mergers by LW97a and 2D turbulence simulations (e.g., Overman and Zabusky 1982; McWilliams 1984; Dritschel and Waugh 1992; Waugh 1992). Many of these studies also have shown that the peak (or more generally, the area averaged) vertical vorticity of a vortex resulting from a merger is approximately the same amplitude as its most intense parent, while its circular diameter is greater than the largest. Therefore, its circulation,

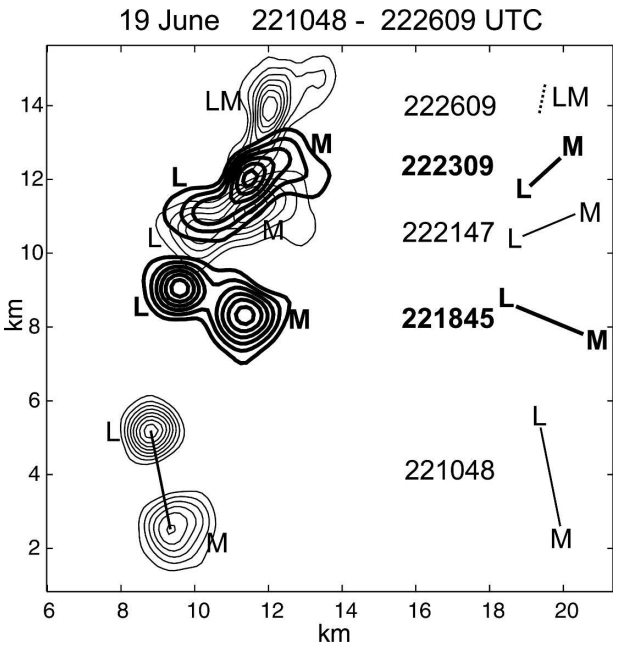

FIG. 7. Contours of vertical vorticity during the merger of misocyclones L and M at five consecutive times along the dryline on 19 Jun. The outermost contour at each time is 5×10^{-3} s^{-1}, incremented by 3×10^{-3} s^{-1}. The merger axis between L and M connects the vorticity cores at 2210:48 UTC and its orientation at each time is shown on the rhs.

$$\Gamma = \iint \zeta \, dx \, dy = \oint \mathbf{v} \cdot d\mathbf{s}, \tag{1}$$

is greater than that around either one of the two merging vortices prior to their interaction. Many of the IHOP misocyclones are observed to intensify before, during, and after a merger because of their collocation with mesoscale convergence and vertical motion. This fact, along with the difficultly in assessing the frictional dissipation of vorticity in our observations, makes it difficult to assess the 2D conservation of circulation during a merger. Unlike Dritschel and Waugh (1992) and Waugh (1992), there are no observations of misocyclones reflecting away from each other as they collide, and there are only a few examples in which vorticity from both misocyclones does not fully coalesce (although even in those cases only a small amount of vorticity remains distinct from the consolidated misocyclone, e.g., L′ for the time shown in Fig. 6f). Instead, most like-signed vorticity patches readily consolidate when they are in close proximity to one another, likely influenced by the mesoscale convergence at the boundary.

As previously mentioned, high-amplitude boundary inflections are sometimes associated with merging misocyclones (e.g., Figs. 1–3, 6). Another example of this

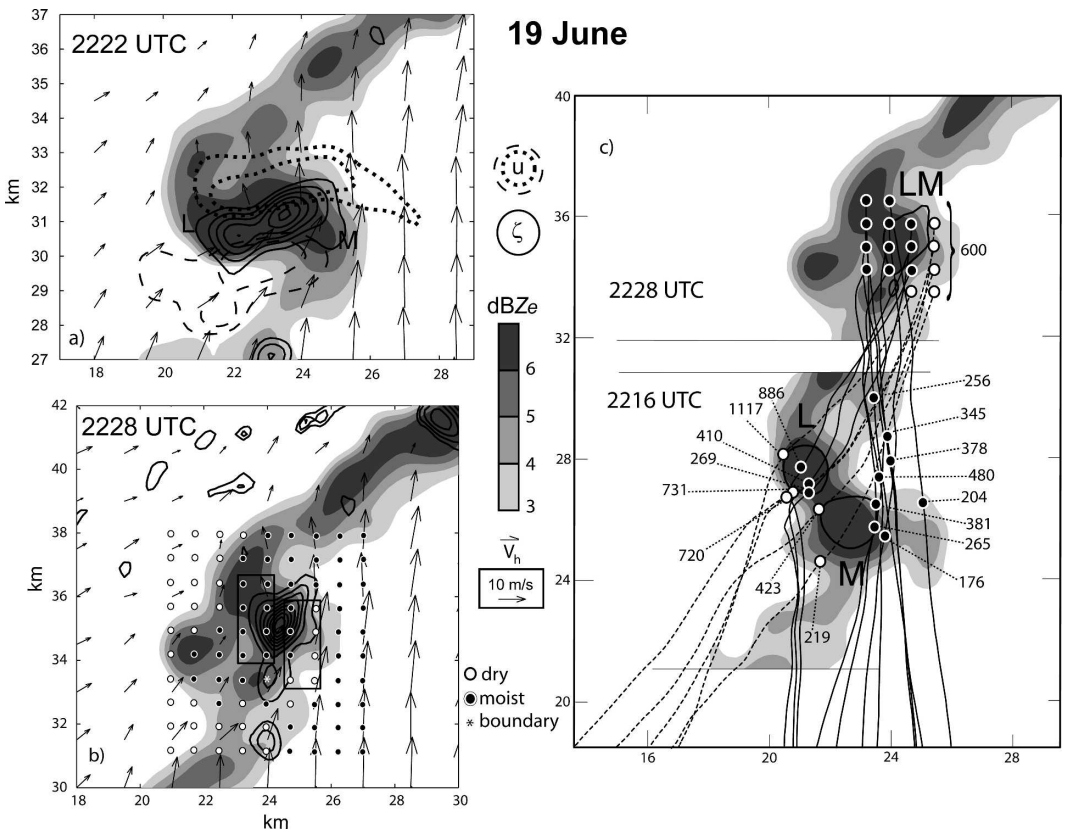

FIG. 8. Vertical vorticity (solid contours), radar reflectivity (shaded), and ground-relative wind (vectors) at z = 300 m AGL at (a) 2222 and (b) 2228 UTC 19 Jun. The outermost contour of vertical vorticity is 5×10^{-3} s^{-1}, incremented by 3×10^{-3} s^{-1}. Also shown in (a) are $u = -2$ and -1 m s^{-1} (dotted), and $u = 6.5$ and 7.5 m s^{-1} (dashed). A grid of parcels at z = 600 m AGL is shown in (b). Parcel origins are marked with dark circles for the moist air mass, white circles for the dry air mass, or asterisks for within the reflectivity contours shown. (c) A horizontal plane projection of the trajectories for the 16 parcels surrounded by rectangles in (b). Parcel positions and altitudes (m), radar reflectivity, and $\zeta = 8 \times 10^{-3}$ s^{-1} are shown at (top) 2228 and (bottom) 2216 UTC. Approximately 25 min of the backward integration of trajectories (starting at 2228 UTC) are shown. Parcel trajectories that originate in the dry air mass are dashed.

is seen during the merger of misocyclones L and M, previously depicted in Figs. 6d–f and shown in greater detail in Fig. 8. In Fig. 8a, a high-amplitude radar reflectivity inflection is centered at the midpoint of the merger axis. This high-amplitude inflection is associated with the increased length scale of the circulation in the across-boundary direction; an approximately 4-km-long jet of the easterly (westerly) wind component is located in the reflectivity minimum just north (south) of the merging pair. A high-amplitude reflectivity inflection does not occur when the merger axis is oriented parallel to the boundary during most of the merger process because the increased length scale of the circulation is not aligned in the across-boundary direction. As the merger of L and M concludes, the boundary inflection collapses and moist (dry) parcel trajectories (integrated backward from 2228 UTC for ~1 h using a fourth-order Runge–Kutta scheme) end in the dry (moist) air mass to the west (east) of the dryline (Fig. 8b). This is further illustrated by the crossing parcel trajectory traces between 2216 and 2228 UTC (Fig. 8c), which differ from the confluent trajectory traces that one might expect along a boundary with no misocyclones. This indicates that thermodynamic mixing across the boundary might be strongly enhanced near merging misocyclones. Crossing trajectory traces also are observed near individual misocyclones (e.g., by misocyclone L just south of its position at 2216 UTC in Fig. 8c) and may lead to moist (dry) air north (south) of a misocyclone along the dryline as observed with airborne lidar (Murphey et al. 2006). An analysis of the mixing of thermodynamic fields by individual and merging misocyclones will be conducted in a future study.

c. Interactions with PBL structures

All three of the IHOP misocyclone datasets contain linear horizontal structures (LHSs) and/or cellular structures in the PBL away from each boundary. A wide variety of environmental processes can force linear structures in the PBL (Young et al. 2002), such as convective plumes organized by wind or shear (e.g., horizontal convective rolls), gravity wave activity, inflection point instability (e.g., Strensrud and Shirer 1988), Kelvin–Helmholtz instability, and so on. It is possible that the LHSs observed in the present datasets are manifestations of one or more of these phenomena (A06; SM07). It is also possible that the cellular structures observed are evidence of open cellular convection or even superimposed LHSs of varying orientation. While the PBL structures are not always ideally retained for quantitative analysis in the final gridded volumes, their qualitative structure is verified with single-Doppler data. During transitions between linear and cellular PBL structures (transition time scale ~1 h), no net production or extinction of misocyclones is observed.

1) INTERACTIONS WITH LINEAR STRUCTURES

Similar to the horizontal convective rolls in W92, several LHSs intersect the dryline on 19 June in close proximity to or even in direct contact with many misocyclones. For a short duration, LHSs from both sides of the dryline are observed to contact it and some misocyclones. Despite this, the degree to which intersections between LHSs and the boundary (LHSIs) are necessary for the existence of the IHOP misocyclones is unclear. One method to determine whether an LHSI is a site for continuous misocyclone presence is to determine if both the LHSIs and misocyclones are moving along the boundary at the same speed. In a single-Doppler radar sequence from 19 June (Fig. 9), misocyclones undergo a series of mergers that significantly accelerate their motion along the dryline. As these interactions take place, many LHSIs in close proximity to one misocyclone from a merging pair are left behind when the merger is complete (e.g., LHS 1 with misocyclones C and D, 2 with E and F, and 4 with G and H). A similar trend is also seen on 3 and 10 June. Unfortunately, high-quality clear-air radar data do not extend to sufficiently high altitudes in any dataset to allow us to see whether horizontal vorticity associated with the LHS activity is directly connected to the misocyclones (e.g., Atkins et al. 1995; Weckwerth and Wakimoto 1992) or whether these horizontal vortex lines interact as merging misocyclones interact. There is also some difficulty distinguishing LHSs near each of the boundaries, as in W92.

As in many other studies, LHSIs are often observed to be regions of enhanced convergence (some examples are found in Fig. 10a). We do not observe the formation of misocyclones along the fairly small portions of each boundary (approximately 10–20 km) seen with the radars; therefore, it is impossible to tell whether the vertical stretching of mesoscale vertical vorticity along each boundary produces vorticity maxima as in Crook et al. (1991) and W92. However, a few preexisting misocyclones located near LHSIs are observed to intensify within the pocket of enhanced low-level convergence.

Linear patterns of alternating positive and negative vertical vorticity associated with the LHSs are observed near the surface in all three datasets. An example of such a vorticity pattern in the dry air mass of 19 June is shown in Fig. 10. The vorticity pattern seems consistent with what one might expect to result from the tilting of horizontal vorticity by alternating lines of upward motion (low-level convergence) and downward motion (low-level divergence) associated with the LHSs (Fig. 10a). The lines of alternating positive and negative vertical vorticity extend into the mesoscale convergence at the dryline, indicating that the LHSs indirectly supply it with vorticity. Similar observations are made with LHSs in the cold air masses on 3 and 10 June.

A rare, intense misoanticyclone, labeled with an "X" throughout Fig. 10, reaches a peak vertical vorticity of approximately -16×10^{-3} s^{-1} at 2208 UTC. Interestingly, X is the only negatively signed vertical vorticity patch located within the dryline at 2147 UTC (Figs. 10a,b) that survives until 2208 UTC (Fig. 10c), and is one of the few negative vorticity cores from all three datasets to persist within any boundary zone for longer than 3–5 min. The merger of GH and IJK induces a strong jet of southeasterly winds to its north at 2208, resulting in a local reversal of the horizontal shear at the dryline such that anticyclonic vorticity is present. Misoanticyclone X develops in this region and reaches maximum intensity when the merger axis of GH and IJK is oriented in a direction that is perpendicular to the dryline. Unfortunately, X propagates out of the observed domain just after GH and IJK fully merge into GHIJK, making it impossible to know if it survives after the kink in the dryline relaxes. It is unclear if the production of misoanticyclone X is forced by the anticyclonic vertical vorticity of the alternating LHS pattern at 2147 UTC or instead is caused by the vertical stretching of the locally reversed across-boundary horizontal shear owing to the merger of GH and IJK.

2) INTERACTIONS WITH CELLULAR STRUCTURES

Cellular structures in the PBL are observed for some duration of all three datasets. At these times, patches of

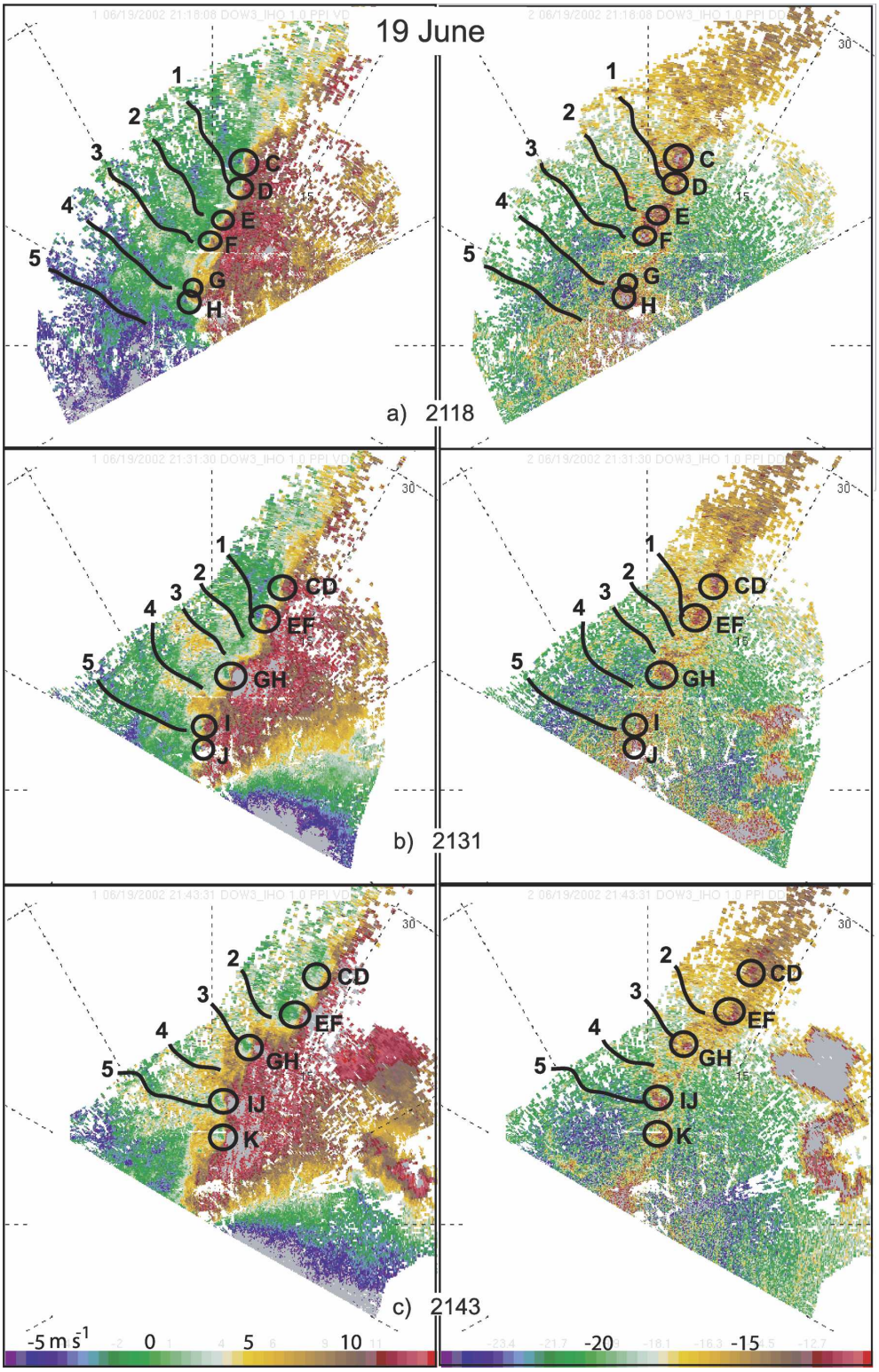

FIG. 9. (left) Radial velocity and (right) reflectivity from DOW 3 at (a) 2118, (b) 2131, and (c) 2143 UTC 19 Jun. LHSs are traced with boldface lines and labeled with numbers, and misocyclones are highlighted with boldface circles and labeled consistently with Fig. 6.

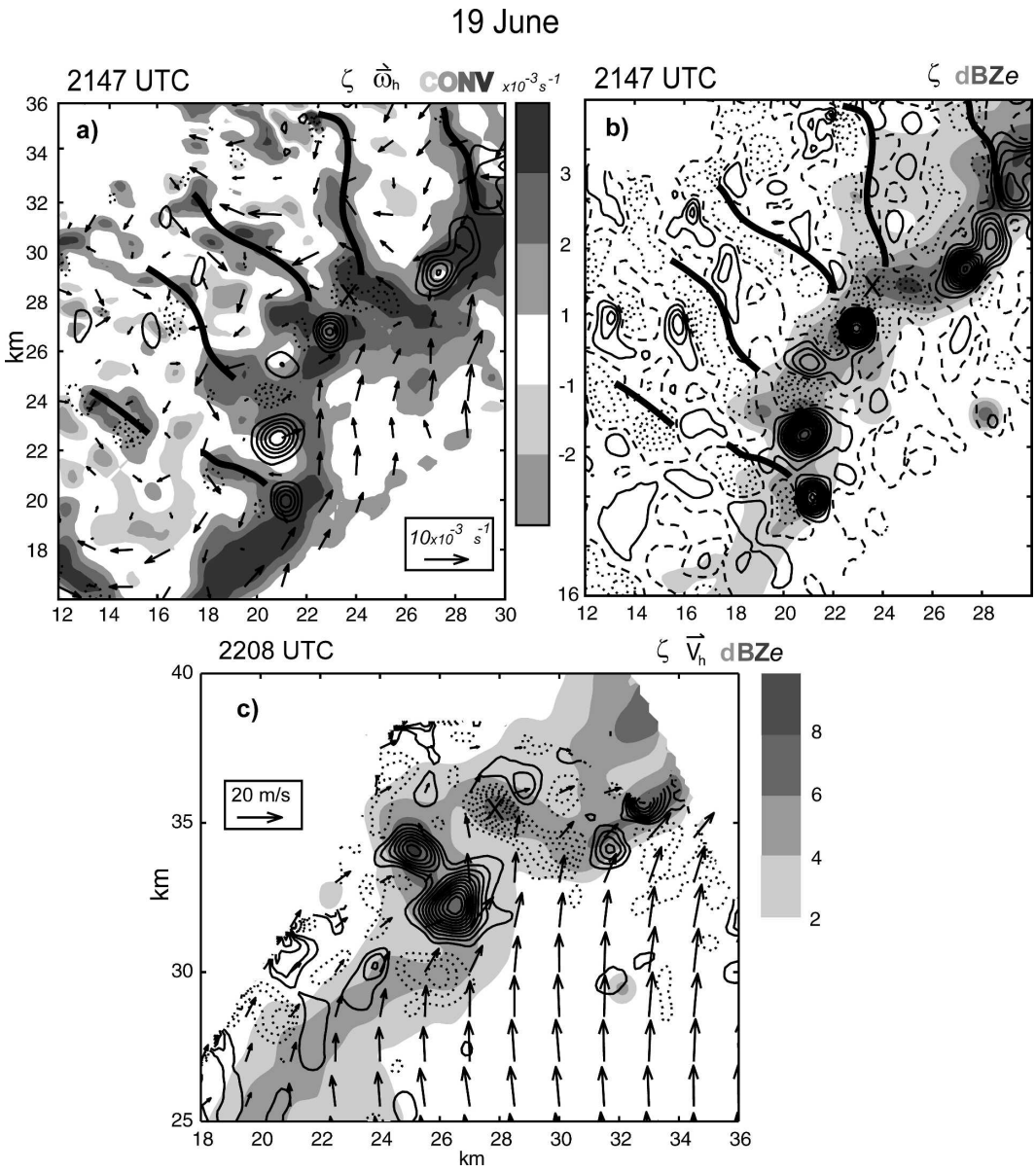

FIG. 10. (a) Vertical vorticity (contours) and convergence (shaded) at 300 m AGL, and horizontal vorticity (vectors) at 750 m AGL at 2147 UTC. The outermost negative ζ contour (dotted) is -4×10^{-3} s^{-1}, incremented by -2×10^{-3} s^{-1}, the outermost positive ζ contour (solid) is 4×10^{-3} s^{-1}, incremented by 4×10^{-3} s^{-1}. (b) Vertical vorticity (contours) and reflectivity (shaded) at 300 m AGL for the same time as in (a). The $\zeta = 0$ contour is dashed, negative values are dotted, and increments are 2×10^{-3} s^{-1}. The boldface lines in (a) and (b) indicate regions of convergence associated with the LHSs. (c) Same as in (b) but at 2208 UTC with ground-relative wind (vectors) and no $\zeta = 0$ contour.

cyclonic vertical vorticity generated by PBL cell structures travel toward the boundary and are often intercepted by misocyclones along it. A few select patches of cyclonic vertical vorticity generated by cellular convection in the moist PBL on 19 June are tracked in Fig. 11 until they are incorporated into the dryline or merge with misocyclones. Anticyclonic vertical vorticity patches traveling into the dryline from cellular PBL sources do not retain their amplitude for a significant period of time, presumably influenced by the mesoscale cyclonic horizontal shear there. In general, the intensity of these anticyclonic patches decreases when they reach close proximity to the mesoscale convergence zone, resulting in a paucity of negative vorticity patches in this area (as in Fig. 11). The exceptions to this behavior are anticyclonic patches that enter the boundary in close

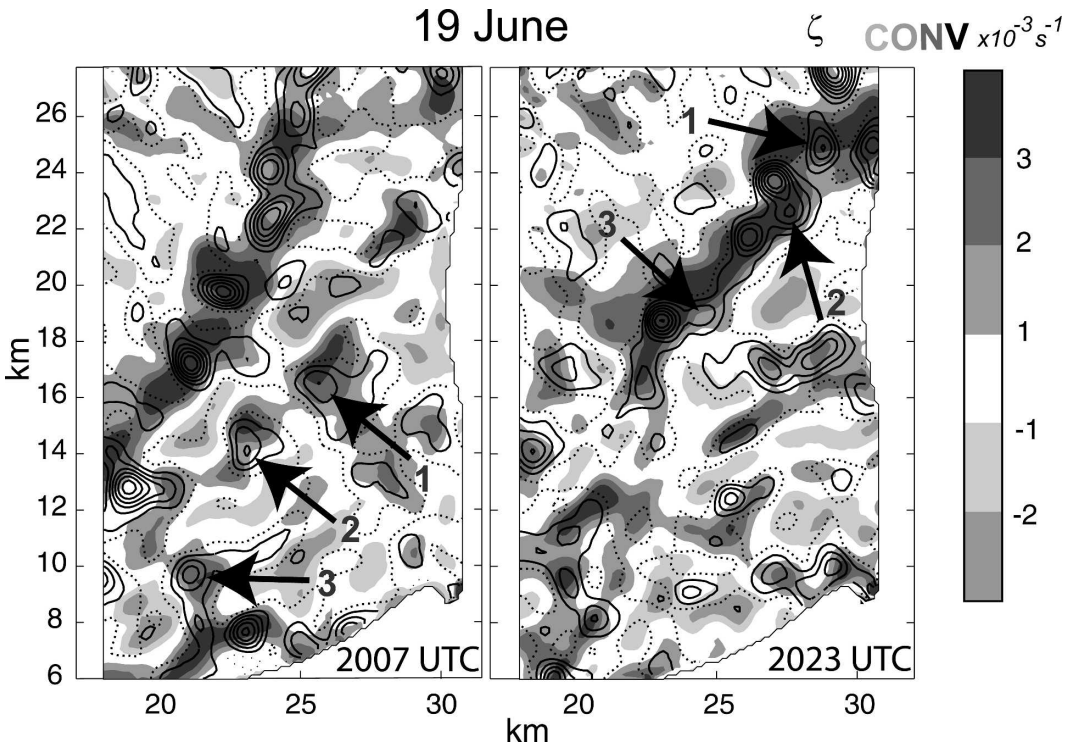

FIG. 11. Vertical vorticity (contours) and convergence (shaded) at 300 m AGL at (left) 2007 and (right) 2023 UTC 19 Jun. Vorticity contours are incremented by 2×10^{-3} s^{-1}; $\zeta = 0$ is dotted. Arrows indicate the positions of three cyclonic vorticity patches at both times.

proximity to large or merging misocyclones. This seems consistent with the behavior described above for misoanticyclone X. In addition, similar to LHSIs, locally enhanced low-level convergence is present at the boundary where patches of convergence associated with PBL cells intersect it, and examples are found in which small, weak, and generally insignificant misocyclones are invigorated at locations where convergence and vorticity patches from PBL cells reach close proximity to a boundary.

d. Misocyclone environments

LW97a show that strong values of the across-boundary shear of the component of wind in the along-boundary direction result in a strong vortex sheet at the gust front, which yields strong misocyclones. They also show that misocyclone strength is related to vertical ambient shear and neutral layer depth because of the roles these play in organizing the structure of the leading edge of the cold pool; however, it is unclear how to adapt these two findings to our three IHOP boundaries because they are not gust fronts. Additionally, it is difficult to compare these two parameters based on only three samples, each with differing thermodynamic characteristics. Therefore, we only examine the average across-boundary differential of the along-boundary wind component ($\Delta\overline{u'}$) and the along-boundary average of the convergence ($\overline{\text{Conv}}$), two parameters that are common to all types of wind-shift boundaries and possibly affect misocyclone strength. Large values of $\overline{\text{Conv}}$ along a mesoscale boundary presumably enhance misocyclone strength by increasing the stretching and/or tilting production of vertical vorticity. However, it should be noted that values of $\overline{\text{Conv}}$ inescapably contain pockets of misocyclone-enhanced convergence along the boundary, contaminating the correlation between environmental mesoscale convergence and $\overline{\text{Conv}}$. The $\Delta\overline{u'}$, $\overline{\text{Conv}}$, and average of the peak vertical vorticities for all misocyclones stronger than 5×10^{-3} s^{-1} ($\overline{\zeta_{\max}}$) are assessed at roughly 20–50-min intervals (data permitting) throughout each dataset at $z = 300$ m. The three datasets are objectively reanalyzed using the smoothing conditions applied to 19 June (that with the coarsest spatial resolution) in order to retain the same scales across each of them. The results, along with daily averages of each parameter, are shown in Fig. 12. The method used to calculate $\Delta\overline{u'}$ and $\overline{\text{Conv}}$ is provided in an appendix. The differential of $\overline{u'}$ is presented rather than its shear ($\partial\overline{u'}/\partial y'$) for reasons that are also discussed in the appendix.

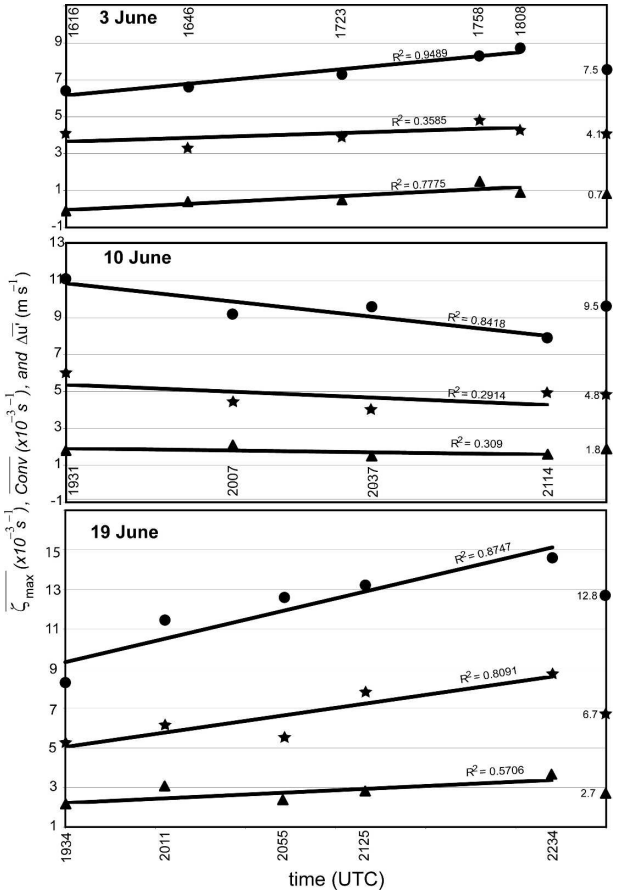

FIG. 12. The $\overline{\zeta_{max}}$ (circles), $\Delta\overline{u'}$ (stars), and $\overline{Conv}$ (triangles) for all times measured on (top) 3, (middle) 10, and (bottom) 19 Jun. The times of each observation are labeled in UTC. Linear regression fits and the associated squared correlation coefficients (R^2) are shown for each time series. The daily average of each parameter for each day is included on the rhs of each panel.

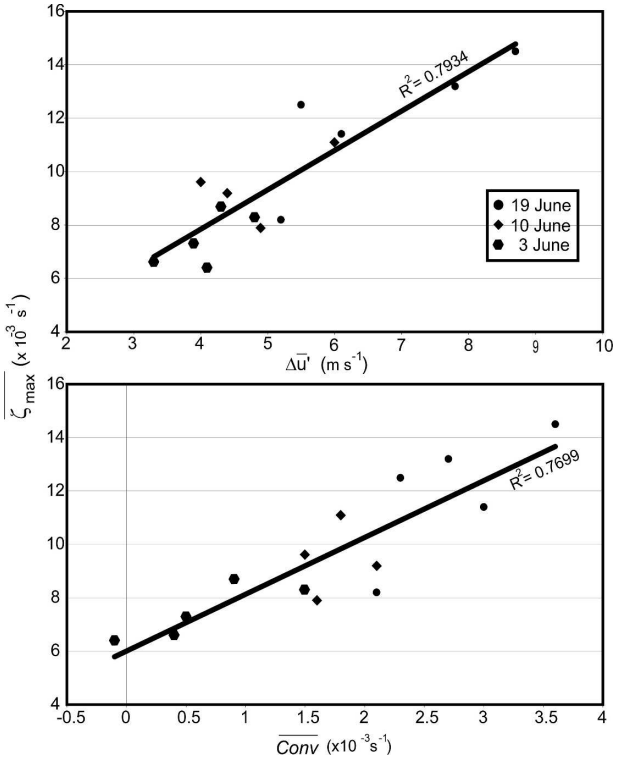

FIG. 13. Linear correlations between (top) $\overline{\zeta_{max}}$ and $\Delta\overline{u'}$ and between (bottom) $\overline{\zeta_{max}}$ and $\overline{Conv}$ using the observations from all three datasets.

The greatest daily average value of $\overline{\zeta_{max}}$ occurs on 19 June, the weakest occurs on 3 June, and an intermediate value occurs on 10 June. There is a similar trend in both $\Delta\overline{u'}$ and $\overline{Conv}$, suggesting possible relationships between these parameters and misocyclone strength. The linear regression *R*-squared (i.e., square of the correlation coefficient) values between $\overline{\zeta_{max}}$ and $\Delta\overline{u'}$ and between $\overline{\zeta_{max}}$ and $\overline{Conv}$ for all observations (Fig. 13) are 0.7934 and 0.7699, respectively, and further support these relationships.

The seemingly simple and intuitive relationships between $\overline{\zeta_{max}}$, $\Delta\overline{u'}$, and $\overline{Conv}$ become complicated when their evolution during each day is considered. It is unknown if changes in the strength of existing misocyclones by evolving mesoscale shear is an expected behavior, as the authors are unaware of any relevant studies. The time trends of $\Delta\overline{u'}$ and $\overline{Conv}$ during all 3 days generally mimic those of $\overline{\zeta_{max}}$, at least in the sense that the slopes of the linear regression lines for each (shown in Fig. 12) have the same sign. However, the linear regression *R*-squared values (also shown in Fig. 12) for neither $\Delta\overline{u'}$ nor $\overline{Conv}$ consistently resemble those for $\overline{\zeta_{max}}$ versus time in any one dataset. It is possible the variations in these quantities on any 1 day are too small, particularly on 3 and 10 June, to uncover the relationships that become obvious when one considers all three cases together, spanning a much wider range of values.

Because no vortex-sheet roll up is observed, it is impossible to be certain if horizontal shear controls misocyclone strength by the same physical mechanism that it does in LW97a. The evolution of $\Delta\overline{u'}$ throughout each day implies that it might be unwise to assume that its value at any particular analysis time is representative of the horizontal shear across a presumed "original" vortex sheet, further complicating the implication of shearing instability as a formation mechanism. Values of $\overline{\zeta_{max}}$ from any one time use the peak vorticity of misocyclones in various stages of evolution. As such, it is assumed that the values over the population represent an average sense of misocyclone intensity. Individual misocyclones are observed to intensify or weaken because of locally strong pockets of low-level convergence or divergence (MH06) on time scales much faster than

those of the evolving mesoscale environment. Therefore, the complexity due to temporal evolution and submesoscale variability, and the small sample size make it difficult to definitively correlate horizontal shear or line-averaged convergence with overall misocyclone strength, although a strong association is suggested at the resolved scales of motion in our objective analysis.

4. Summary and conclusions

Misocyclones occurring along three mesoscale boundaries observed during IHOP (3, 10, and 19 June) are examined with dual- and multi-Doppler radar-derived wind fields. The fine temporal and spatial resolution data permit the tracking of individual misocyclones and reveal certain phenomena seldom observed. These include the relationship between low-level convergence and misocyclones, the merger of misocyclones, and the interplay between misocyclones and linear and cellular structures observed in the planetary boundary layer. Properties of the mesoscale environmental airflow from each dataset are examined to determine if any clear relationships with misocyclone strength exist.

Most of the observed misocyclones exhibit similar traits: vertical vorticity that decreases with height, quasi-circular vorticity contours (in a horizontal plane), radar reflectivity maxima surrounding the center of rotation, and inflections of the fine-line reflectivity signature centered on the misocyclones. Many misocyclones contain minimized low-level convergence in their cores, likely due to the negative vertical gradient of the magnitude of vertical vorticity. Misocyclones of different core radii are observed to distort the linear swath of low-level convergence along the boundary to varying degrees. If a misocyclone is large (small) relative to the width of mesoscale convergence, then the boundary in its vicinity is highly (weakly) inflected or distorted. When misocyclone neighbors are each distorting the low-level convergence, they can create a staircase shape along the span of the boundary. The mesoscale convergence field along a boundary containing misocyclones of the different sizes and arrangements reported in this study is conceptualized in Fig. 14.

The consolidation of neighboring misocyclones is a common occurrence along all three of the boundaries reported in this study. In general, vertical vorticity maxima (e.g., misocyclones and PBL vorticity patches) are observed to readily merge when they are in close proximity regardless of their sizes or intensities. The core diameter of a misocyclone that results from a merger is at least slightly larger than that of the largest of the merging pair. Through a series of mergers, a population composed of numerous small misocyclones transforms into fewer larger misocyclones, consistent with the primary findings of LW97a and 2D studies of vortices. During a merger, the boundary is contorted differently depending on the alignment of the consolidating misocyclone pair. When the merger axis of a neighboring pair is aligned perpendicular to the overall orientation of the boundary, a high-amplitude boundary inflection is observed. A much lower-amplitude inflection occurs when the two merging misocyclones are aligned along the boundary. This might have implications for buoyant mixing across the boundary. Fine spatial and temporal resolutions are of paramount importance to the observation of misocyclone mergers because their time scales are typically less than 15 min and often as short as 5 min.

Both cellular and linear structures are observed in the planetary boundary layers of each dataset. Vertical vorticity with origins from both of these PBL structures is found within the boundary zone. Misocyclones often ingest the PBL-born cyclonic vertical vorticity patches as they approach the boundary nearby, similar to mergers with misocyclone neighbors. Anticyclonic vertical vorticity patches injected into the boundary zone by the PBL structures rarely persist, except near large misocyclones or merging pairs that are aligned in the across-boundary direction where there exists localized anticyclonic across-boundary horizontal shear. Enhanced low-level convergence is found at the intersections of linear and cellular PBL structures and the boundary, and misocyclones are observed to intensify in their vicinity. We do not observe the *formation* of any misocyclones at LHS-boundary intersections (W92; Crook et al. 1991) within the radar domain. However, the persistent injection of vertical vorticity into the boundary zone suggests that the linear and cellular structures in the PBL could play a role in the formation of the IHOP misocyclones. The evolution from linear to cellular structure (or vice versa) as viewed in the relatively small radar domains does not yield drastic changes in misocyclone strength or organization. Numerical models that include changes in convective PBL structure (e.g., Peckham et al. 2004) might provide a better means to study this interaction.

The greatest (weakest) average peak misocyclone intensity occurs on the same day as the greatest (weakest) across-boundary horizontal shear and greatest (weakest) along-boundary average of low-level convergence—an intuitive relationship. However, the temporal evolution of these parameters complicates the comparison of the horizontal shear mechanism with that of LW97a because we do not definitively know the

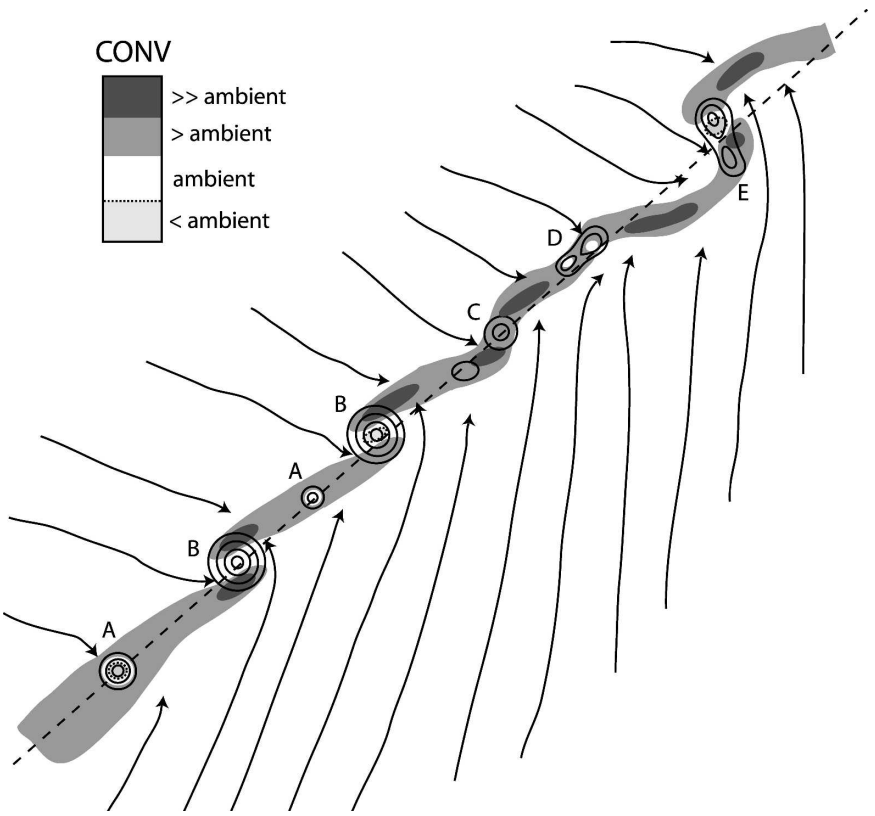

FIG. 14. Conceptual illustration of misocyclones (ζ greater than an ambient value is contoured), convergence (shaded), and streamlines along the three IHOP boundaries. The misocyclones at both A positions are small relative to the average width of mesoscale convergence. The misocyclones at both B positions are large compared with the width of mesoscale convergence. The misocyclone at position C has a width similar to that of the convergence at the boundary. Merging misocyclones aligned with the boundary and oriented perpendicular to the boundary are located at positions D and E, respectively.

strength of an "initial" vortex sheet present at the boundary. Misocyclones are present at the first analysis time of all three datasets; therefore, it is impossible to know with certainty whether horizontal shearing instability is involved with their formation.

During our analysis, certain questions have arisen.

1) How do the environmental parameters analyzed in LW97a affect the formation and behavior of misocyclones along weak fronts, drylines, and so on, where density current dynamics are presumed to less strongly govern boundary structure than is true for storm-induced gust fronts?
2) How does the evolution of the mesoscale environment affect the evolution of misocyclone strength?
3) What conditions favor an enhancement of vertical motion along a boundary upstream and/or downstream of a misocyclone?
4) Are sites near merging misocyclones favorable for convection initiation?

If future studies are able to address the questions posed here, we will likely have a better understanding of how misocyclones vary by environment and under what conditions they might affect convective development, facilitating the increased skill of thunderstorm and nonsupercell tornado forecasts.

Acknowledgments. This study was funded by NSF Grants ATM-0208651, ATM-0336712, and ATM-0437505. We are extremely thankful to Paul Markowski, Nettie Arnott, and Brian Monahan for the writing of and assistance with radar synthesis scripts, to P. Markowski, N. Arnott, John Stonitsch, and Chris Hartman for providing radar observations and analysis opinions, to Bruce Lee for his helpful clarifications and encouragement, and to all who aided the collection of the 3, 10, and 19 June 2002 DOW, XPOL, and SMART radar datasets during IHOP. We also thank Conrad Ziegler and two anonymous reviewers for their helpful comments and the authors of the SOLOII, REOR-

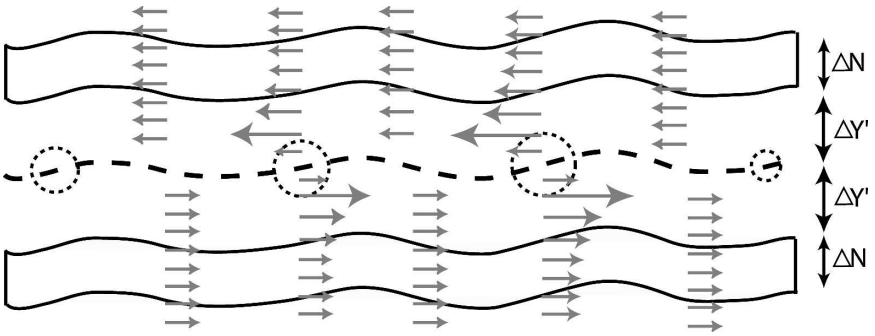

FIG. A1. Schematic illustration of the 2D averaging area in relation to each boundary that is used to calculate $\overline{u'}$ from u' (the latter vector field is shown in a misocyclone-relative frame). Heavy dashed line is the maximum in $|\nabla \mathbf{v}|_h$ along the boundary, and the dashed circles represent the approximate radius of peak horizontal wind in each misocyclone.

DER, CEDRIC, and Vis5D routines that were used extensively in this study. In addition to the coauthors, J. Marquis would like to thank the other members of his M.S. thesis committee: P. Markowski and Peter Bannon for their helpful comments with an earlier version of this manuscript.

APPENDIX

Method to Calculate Horizontal Shear and Convergence at Each Boundary

Values of $\overline{u'}$ used in the calculation of $\Delta\overline{u'}$ are found in the following manner. The wind field is rotated such that the mesoscale orientation of the boundary segment is aligned in the east–west ($\hat{x}'$) direction. Kinks and inflections in a boundary caused by misocyclone circulations are straightened by aligning the maximum values of the horizontal velocity gradient tensor (SM07),

$$|\nabla \mathbf{v}|_h = \sqrt{\frac{1}{2}\left[\left(\frac{\partial u'}{\partial x'}\right)^2 + \left(\frac{\partial u'}{\partial y'}\right)^2 + \left(\frac{\partial v'}{\partial x'}\right)^2 + \left(\frac{\partial v'}{\partial y'}\right)^2\right]}, \quad \text{(A1)}$$

in each column ($\hat{y}'$) of data (u' and v' are the east–west and north–south components, respectively, of the rotated wind field). The area average of u' is then performed within a 2D box on both sides of the boundary, defined by the length of the boundary segment (in the $\hat{x}'$ direction) and a width, ΔN, in the $\hat{y}'$ direction. Here ΔN is assigned a value of 4 km, the largest width permissible in the smallest of all of the radar domains. The closest edge of the averaging box to the boundary in each air mass is deliberately located a certain distance, $\Delta Y'$, away from the straightened maximum of $|\nabla \mathbf{v}|_h$ in order to prevent misocyclone-induced contributions of u' in the calculation of $\overline{u'}$ (which could lead to artificially high correlations between $\Delta\overline{u'}$ and vortex strength). The $\Delta Y'$ chosen is the e-folding distance of the radial tangential wind profile outside of the core region of a rankine vortex, $u(r) = u_{\max}(R/r)$, where $u_{\max}$ and R are maximum tangential wind and the radius of maximum tangential wind, respectively. The Rankine tangential wind profile used to calculate the $\Delta Y'$ is based on the largest misocyclone observed in all three datasets (R = 1.0 km), yielding $\Delta Y'$ = 2.7 km. For clarity, Fig. A1 schematically illustrates the dimensions of the averaging box used to calculate $\overline{u'}$. The differential of $\overline{u'}$ is calculated rather than its shear ($\partial\overline{u'}/\partial y'$, or $\Delta\overline{u'}/\Delta y'$) because of the somewhat arbitrary choice of both $\Delta Y'$ and ΔN. Here, $\overline{\text{Conv}}$ is found by averaging the largest value of ($\partial u'/\partial x' + \partial v'/\partial y'$) along each x' value within 2 km of the maximum value of $|\nabla \mathbf{v}|_h$.

REFERENCES

Arnott, N., Y. Richardson, J. Wurman, and J. Lutz, 2003: A solar calibration technique for determining mobile radar pointing angles. Preprints, *31st Int. Conf. on Radar Meteorology,* Seattle, WA, Amer. Meteor. Soc., CD-ROM, P3C.12.

——, Y. Richardson, J. Wurman, and E. M. Rasmussen, 2006: Relationship between a weakening cold front, misocyclones, and cloud development on 10 June 2002 during IHOP. *Mon. Wea. Rev.,* **134,** 310–334.

Atkins, N. T., R. M. Wakimoto, and T. M. Weckwerth, 1995: Observations of the sea-breeze front during CaPE. Part II: Dual-Doppler and aircraft analysis. *Mon. Wea. Rev.,* **123,** 944–969.

Barnes, S. L., 1964: A technique for maximizing details in numerical weather map analysis. *J. Appl. Meteor.,* **3,** 396–409.

Biggerstaff, M. I., and J. Guynes, 2000: A new tool for atmospheric research. Preprints, *20th Conf. on Severe Local Storms,* Orlando, FL, Amer. Meteor. Soc., 277–280.

——, and Coauthors, 2005: The Shared Mobile Atmospheric Research and Teaching Radar: A collaboration to enhance research and teaching. *Bull. Amer. Meteor. Soc.,* **86,** 1263–1274.

Bluestein, H. B., and A. L. Pazmany, 2000: Observations of tornadoes and other convective phenomena with a mobile 3-mm wavelength, Doppler radar: The spring 1999 field experiment. *Bull. Amer. Meteor. Soc.,* **81,** 2939–2951.

Brady, R. H., and E. J. Szoke, 1989: A case study of nonmesocy-

clone tornado development in northeast Colorado: Similarities to waterspout formation. *Mon. Wea. Rev.,* **117,** 843–856.

Carbone, R. E., 1982: A severe frontal rainband. Part I: Stormwide hydrodynamic structure. *J. Atmos. Sci.,* **39,** 258–279.

——, 1983: A severe frontal rainband. Part II: Tornado parent vortex circulation. *J. Atmos. Sci.,* **40,** 2639–2654.

Christiansen, J. P., and N. J. Zabusky, 1973: Instability, coalescence and fission of finite-area vortex structures. *J. Fluid Mech.,* **61,** 219–243.

Crook, N. A., T. L. Clark, and M. W. Moncrieff, 1991: The Denver cyclone. Part II: Interaction with the convective boundary layer. *J. Atmos. Sci.,* **48,** 2109–2126.

Davies-Jones, R. P., 1985: Comments on "A kinematic analysis of frontogenesis associated with a nondivergent vortex." *J. Atmos. Sci.,* **42,** 2073–2075.

Doswell, C. A., III, 1984: A kinematic analysis of frontogenesis associated with a nondivergent vortex. *J. Atmos. Sci.,* **41,** 1242–1248.

Dowell, D. C., C. R. Alexander, J. M. Wurman, and L. J. Wicker, 2005: Centrifuging of hydrometeors and debris in tornadoes: Radar-reflectivity patterns and wind-measurement errors. *Mon. Wea. Rev.,* **133,** 1501–1524.

Dritschel, D. G., and D. W. Waugh, 1992: Quantification of the inelastic interaction of unequal vortices in two-dimensional vortex dynamics. *Phys. Fluids,* **4,** 1737–1744.

Forbes, G. S., and R. M. Wakimoto, 1983: A concentrated outbreak of tornadoes, downbursts, and microbursts, and implications regarding vortex classification. *Mon. Wea. Rev.,* **111,** 220–236.

Friedrich, K., D. Kingsmill, and C. R. Young, 2005: Misocyclone characteristics along Florida gust fronts during CaPE. *Mon. Wea. Rev.,* **133,** 3345–3367.

Fujita, T. T., 1981: Tornadoes and downbursts in the context of generalized planetary scales. *J. Atmos. Sci.,* **38,** 1511–1534.

Fujiwhara, S., 1931: Short note on the behavior of two vortices. *Proc. Phys. Math. Soc. Japan,* **13,** 106–110.

Kessinger, C. J., P. S. Ray, and C. E. Hane, 1987: The Oklahoma squall line of 19 May 1997. Part I: A multiple Doppler analysis of convective and stratiform structure. *J. Atmos. Sci.,* **44,** 2840–2864.

——, D. B. Parsons, and J. Wilson, 1988: Observations of a storm containing misocyclones, downbursts, and horizontal vortex circulations. *Mon. Wea. Rev.,* **116,** 1959–1982.

Kingsmill, D. E., 1995: Convection initiation associated with a seabreeze front, a gust front, and their collision. *Mon. Wea. Rev.,* **123,** 2913–2933.

Klemp, J. B., and R. Rotunno, 1983: A study of the tornadic region within a supercell thunderstorm. *J. Atmos. Sci.,* **40,** 359–377.

Koch, S. E., M. DesJardins, and P. J. Kocin, 1983: An interactive Barnes objective map analysis scheme for use with satellite and conventional data. *J. Climate Appl. Meteor.,* **22,** 1487–1503.

Lee, B. D., and R. Wilhelmson, 1997a: The numerical simulation of nonsupercell tornadogenesis. Part I: Initiation and evolution of pretornadic misocyclone circulations along a dry outflow boundary. *J. Atmos. Sci.,* **54,** 32–60.

——, and ——, 1997b: The numerical simulation of nonsupercell tornadogenesis. Part II: Evolution of a family of tornadoes along a weak outflow boundary. *J. Atmos. Sci.,* **54,** 2387–2414.

——, and ——, 2000: The numerical simulation of nonsupercell tornadogenesis. Part III: Tests investigating the role of CAPE, vortex sheet strength, and boundary layer vertical shear. *J. Atmos. Sci.,* **57,** 2246–2261.

——, C. A. Finley, and R. B. Wilhelmson, 2000: Simulating deep convection initiation by misocyclones. Preprints, *20th Conf. on Severe Local Storms,* Orlando, FL, Amer. Meteor. Soc., 70–73.

Manin, D. Y., 1992: A study of repeated vortex mergers in a forced quasi-2-D shear flow. *Phys. Fluids,* **4,** 1715–1723.

Markowski, P., and C. Hannon, 2006: Multiple-Doppler radar observations of the evolution of vorticity extrema in a convective boundary layer. *Mon. Wea. Rev.,* **134,** 355–374.

Matejka, T., 2002: Estimating the most steady frame of reference from Doppler radar data. *J. Atmos. Oceanic Technol.,* **19,** 1035–1048.

McWilliams, J. C., 1984: The emergence of isolated coherent vortices in turbulent flow. *J. Fluid Mech.,* **146,** 21–43.

Miles, J. W., and L. N. Howard, 1964: Note on heterogeneous shear flow. *J. Fluid Mech.,* **20,** 331–336.

Mueller, C. K., and R. E. Carbone, 1987: Dynamics of a thunderstorm outflow. *J. Atmos. Sci.,* **44,** 1879–1898.

Murphey, H. V., R. M. Wakimoto, C. Flamant, and D. E. Kingsmill, 2006: Dryline on 19 June 2002 during IHOP. Part I: Airborne Doppler and LEANDRE II analysis of the thin line structure and convection initiation. *Mon. Wea. Rev.,* **134,** 406–430.

Overman, E. A., and N. J. Zabusky, 1982: Evolution and merger of isolated vortex structures. *Phys. Fluids,* **25,** 1297–1305.

Pauley, P. M., and X. Wu, 1990: The theoretical, discrete, and actual response of the Barnes objective analysis scheme for one- and two-dimensional fields. *Mon. Wea. Rev.,* **118,** 1145–1164.

Peckham, S. E., R. B. Wilhelmson, L. J. Wicker, and C. L. Ziegler, 2004: Numerical simulation of the interaction between the dryline and horizontal convective rolls. *Mon. Wea. Rev.,* **132,** 1792–1812.

Pietrycha, A. E., and E. N. Rasmussen, 2004: Finescale surface observations of the dryline: A mobile mesonet perspective. *Wea. Forecasting,* **19,** 1075–1088.

Richardson, Y. P., J. M. Wurman, and C. Hartman, 2003: Multi-Doppler analysis of convective initiation on 19 June 2002 during IHOP. Preprints, *31st Int. Conf. on Radar Meteorology,* Seattle, WA, Amer. Meteor. Soc., 793–795.

Roberts, R. D., and J. W. Wilson, 1995: The genesis of three nonsupercell tornadoes observed with dual-Doppler radar. *Mon. Wea. Rev.,* **123,** 3408–3436.

Stensrud, D. J., and H. N. Shirer, 1988: Development of boundary layer rolls from dynamic instabilities. *J. Atmos. Sci.,* **45,** 1007–1019.

Stonitsch, J., and P. Markowski, 2007: Unusually long-duration, dual-Doppler observations of a front in a convective boundary layer. *Mon. Wea. Rev.,* **135,** 93–117.

Trapp, R. J., and C. A. Doswell III, 2000: Radar data objective analysis. *J. Atmos. Oceanic Technol.,* **17,** 105–120.

——, and M. L. Weisman, 2003: Low-level mesovortices within squall lines and bow echoes. Part II: Their genesis and implications. *Mon. Wea. Rev.,* **131,** 2804–2823.

Wakimoto, R., and J. W. Wilson, 1989: Non-supercell tornadoes. *Mon. Wea. Rev.,* **117,** 1113–1140.

Waugh, D. W., 1992: The efficiency of symmetric vortex merger. *Phys. Fluids,* **4,** 1745–1758.

Weckwerth, T. M., and R. Wakimoto, 1992: The initiation and organization of convective cells atop a cold-air outflow boundary. *Mon. Wea. Rev.,* **120,** 2169–2187.

——, and Coauthors, 2004: An overview of the International H_2O Project (IHOP) and some preliminary highlights. *Bull. Amer. Meteor. Soc.,* **85,** 253–277.

Weisman, M. L., and R. J. Trapp, 2003: Low-level mesovortices within squall lines and bow echoes. Part I: Overview and dependence on environmental shear. *Mon. Wea. Rev.,* **131,** 2779–2803.

Wilson, J. W., 1986: Tornadogenesis by nonprecipitation induced by wind shear lines. *Mon. Wea. Rev.,* **114,** 270–284.

——, G. B. Foote, N. A. Crook, J. C. Fankhauser, C. G. Wade, J. D. Tuttle, and D. K. Mueller, 1992: The role of boundary layer convergence zones and horizontal rolls in the initiation of thunderstorms: A case study. *Mon. Wea. Rev.,* **120,** 1785–1815.

Wurman, J., 2001: The DOW mobile multiple Doppler network. Preprints, *30th Int. Conf. on Radar Meteorology,* Munich, Germany, Amer. Meteor. Soc., 95–97.

——, J. M. Straka, and E. N. Rasmussen, 1996: Preliminary radar observations of the structure of tornadoes. Preprints, *18th Conf. on Severe Local Storms,* San Francisco, CA, Amer. Meteor. Soc., 17–22.

——, ——, E. Rasmussen, M. Randall, and A. Zahrai, 1997: Design and development of a portable, pencil-beam, pulsed, 3-cm Doppler radar. *J. Atmos. Oceanic Technol.,* **14,** 1502–1512.

Young, G. S., D. A. R. Kristovich, M. R. Hjelmfelt, and R. C. Foster, 2002: Rolls, streets, waves, and more: A review of quasi-two-dimensional structures in the atmospheric boundary layer. *Bull. Amer. Meteor. Soc.,* **83,** 997–1001.